Interfacial area measurements for unsaturated flow through a porous medium

Katherine A. Culligan,[1,2] Dorthe Wildenschild,[3,4] Britt S. B. Christensen,[4] William G. Gray,[5] Mark L. Rivers,[6] and Andrew F. B. Tompson[7]

Received 19 April 2004; revised 17 July 2004; accepted 28 September 2004; published 22 December 2004.

[1] Multiphase flow and contaminant transport in porous media are strongly influenced by the presence of fluid-fluid interfaces. Recent theoretical work based on conservation laws and the second law of thermodynamics has demonstrated the need for quantitative interfacial area information to be incorporated into multiphase flow models. We have used synchrotron based X-ray microtomography to investigate unsaturated flow through a glass bead column. Fully three-dimensional images were collected at points on the primary drainage curve and on the secondary imbibition and drainage loops. Analysis of the high-resolution images (17 micron voxels) allows for computation of interfacial areas and saturation. Corresponding pressure measurements are made during the course of the experiments. Results show the fluid-fluid interfacial area increasing as saturation decreases, reaching a maximum at saturations ranging from 20 to 35% and then decreasing as the saturation continues to zero. The findings support results of numerical studies reported in the literature. *INDEX TERMS:* 1875 Hydrology: Unsaturated zone; 1829 Hydrology: Groundwater hydrology; 1894 Hydrology: Instruments and techniques; *KEYWORDS:* interfacial area, porous media, unsaturated flow

Citation: Culligan, K. A., D. Wildenschild, B. S. B. Christensen, W. G. Gray, M. L. Rivers, and A. F. B. Tompson (2004), Interfacial area measurements for unsaturated flow through a porous medium, *Water Resour. Res.*, *40*, W12413, doi:10.1029/2004WR003278.

1. Introduction

[2] Fluid-fluid interfaces distinguish multiphase fluid flow from single-phase fluid flow in porous media. These interfaces play a key role in the dynamics of multiphase flows and contaminant transport in subsurface systems. While traditional macroscale variables such as porosity and saturation are used in the standard continuum description of multiphase flow [e.g., *Bear*, 1972], alone they are insufficient to account for the impact of the fluid-fluid interface on the system. Consequently, the evolution of the interfacial area per volume has come to the forefront as an important component of accurate models of multiphase flow in porous media [*Gray et al.*, 2002].

[3] For a particular value of saturation, numerous corresponding distributions of fluids within the pore space are possible. Additionally, this microscale distribution of fluids impacts the amount of interfacial area available for mass transfer. For example, studies of nonaqueous phase (NAPL) dissolution in porous media have demonstrated that saturation alone is incapable of describing the rate of change of saturation [e.g., *Miller et al.*, 1990; *Powers et al.*, 1992; *Imhoff et al.*, 1994; *Nambi and Powers*, 2000]. Despite no knowledge of the specific interfacial area in the system, an effective rate constant that implicitly combines the effect of interfacial area and the reaction rate constant, is typically used to model mass transfer processes such as NAPL dissolution [*Johns and Gladden*, 1999]. Therefore while not explicitly accounted for, fluid-fluid interfaces are incorporated into mass transfer models. Thus the specific fluid-fluid interfacial area is a particularly important macroscale variable. In fact, incorporation of this parameter into models will be a crucial step in the development of robust simulators that correctly describe mass, momentum, and energy transfer between phases.

[4] In recent years, work has been done to develop a thermodynamically constrained macroscale description of flow in porous media [e.g., *Gray and Hassanizadeh*, 1989; *Bennethum*, 1994; *Gray and Hassanizadeh*, 1998; *Gray*, 1999, 2000; *Gray et al.*, 2002] in which the presence of interfaces is explicitly taken into account. In this approach, mass, momentum, and energy conservation equations are written for the phases and interfaces (and common lines, if desired) at the microscale for a system composed of two fluids and a solid [e.g., *Gray et al.*, 2002]. Averaging theorems [*Gray et al.*, 1993] are applied to transform the microscale equations to the macroscale in a mathematically consistent fashion. The second law of thermodynamics can be similarly transformed from the microscale to the macroscale and then constrained with the macroscale mass, momentum, and energy conservation equations. Application

[1]Department of Civil Engineering and Geological Sciences, University of Notre Dame, Notre Dame, Indiana, USA.
[2]Temporarily at Department of Geosciences, Oregon State University, Corvallis, Oregon, USA.
[3]Department of Geosciences, Oregon State University, Corvallis, Oregon, USA.
[4]Environment and Resources, Technical University of Denmark, Lyngby, Denmark.
[5]Department of Environmental Science and Engineering, University of North Carolina, Chapel Hill, North Carolina, USA.
[6]Consortium for Advanced Radiation Sources and Department of Geophysical Sciences, University of Chicago, Chicago, Illinois, USA.
[7]Geosciences and Environmental Technologies Division, Lawrence Livermore National Laboratory, Livermore, California, USA.

0043-1397/04/2004WR003278$09.00

of this thermodynamically constrained averaging theory approach (TCATA) results in a mathematically rigorous description of multiphase flow in porous media that is consistent with microscale physical processes. For instance, the traditional hysteretic moisture retention function, in which the capillary pressure is taken to be a function of the wetting phase saturation alone, is shown to be incomplete. In fact, the capillary pressure depends on a wide range of macroscopic variables, such as the rate of change of wetting phase saturation, specific fluid-fluid interfacial area, the wetted fraction of the solid surface, and the specific solid interfacial area. *Hassanizadeh and Gray* [1993] hypothesized that the hysteretic nature of the traditional capillary pressure-saturation relationship is, in fact, the result of projecting a very complex capillary pressure function onto a single plane. *Gray et al.* [2002] presented an alternative expression for the capillary pressure based on the TCATA:

$$\frac{D^s \varepsilon^w}{Dt} - x_s^{ws} \frac{D^s \varepsilon}{Dt} = L_s \left(p^w - p^n - \gamma^{wn} J_{wn}^w \right), \tag{1}$$

where D^s/Dt is the material time derivative with respect to the solid phase, ε^w is the volume fraction of the wetting phase, x_s^{ws} is the wetted fraction of the solid surface, ε is the porosity, L_s is a positive coefficient, p^w is the wetting phase pressure, p^n is the nonwetting phase pressure, γ^{wn} is the wetting-nonwetting phase interfacial tension, and J_{wn}^w is the mean macroscale curvature. Note that all variables used in equation (1) are macroscopic. *Gray* [1999] postulated that

$$J_{wn}^w = J_{wn}^w \left(\varepsilon^w, a^{wn}, x_s^{ws}, a^s, \varepsilon \right), \tag{2}$$

where a^{wn} is the wetting-nonwetting interfacial area, and a^s is the solid phase interfacial area, but states that the actual dependence will have to be determined or verified experimentally. Note that films have not been explicitly accounted for in (1) and (2). If the negative product of the interfacial tension and the mean macroscale curvature is identified as the capillary pressure, p^c, then equation (1) provides the standard equilibrium expression for capillary pressure:

$$p^c = p^n - p^w. \tag{3}$$

However, because p^c has been identified as $-\gamma^{wn} J_{wn}^w$, the assumption that the capillary pressure depends on the saturation alone is likely incomplete. Note that J_{wn}^w is a macroscale measure of interfacial curvature and is not a quantity readily available. Ideally, it would be an average curvature of some sort. However, as a surrogate, one might hypothesize that knowledge of both the volume of a fluid present and of the surface area of the interface may be satisfactory. For a sphere, the surface area divided by the volume is equal to 3/2 the curvature, for example. Of course, the relation will not be as simple for a fluid distributed within a porous medium.

[5] *Hassanizadeh and Gray* [1993] state that the hysteresis observed in standard capillary pressure-saturation plots is an artifact of a deficit in the number of independent variables used to model capillarity. In addition, they suggest that of the independent variables missing from the functional form of the capillary pressure, the fluid-fluid interfacial area is the most important. If this is the case, the necessary test is to see if expanding the functional dependence of the capillary pressure to include interfacial area, that is $p^c = p^c(s^w, a^{wn})$, where $\varepsilon^w = \varepsilon s^w$, results in a unique surface. The shape of the $p^c - s^w - a^{wn}$ surface will have to be determined experimentally [*Hassanizadeh and Gray*, 1993].

[6] While fluid-fluid interfacial area per volume is the macroscale quantity of interest for use in emerging theories, such as that described above, and for understanding phenomena such as mass transfer and volatilization in the subsurface, the interfacial area must first be measured at the microscale due to the lack of direct macroscopic measures of fluid-fluid interfacial area. Macroscopic measurements of interfacial area have been estimated in situ indirectly using interfacial tracer techniques [e.g., *Kim et al.*, 1997; *Costanza-Robinson and Brusseau*, 2002], but are uncertain because the portion of the fluid-fluid interface that is accessed by the tracer and included in the resulting measure is unclear. As of yet, there has been no independent validation of the results found using interfacial tracers [*Kim et al.*, 1999]. Heretofore, experimentally measuring the interfacial area at the pore scale has proven to be a difficult task [e.g., *Reeves and Celia*, 1996; *Held and Celia*, 2001]. A number of pore-scale numerical investigations [e.g., *Reeves and Celia*, 1996; *Berkowitz and Hansen*, 2001; *Dalla et al.*, 2002; *Pan et al.*, 2004] have been conducted, and the results used as a surrogate for pore-scale experimental measurements. Nevertheless, it is imperative that research efforts be directed toward the task of physically measuring interfacial areas at the pore scale in order to both calibrate numerical models and substantiate the results obtained from them [*Reeves and Celia*, 1996].

[7] The work presented herein was motivated by the need for a direct measure of interfacial area (on the order of microns) which could then also be used to evaluate existing experimental measures of interfacial area (e.g., interfacial tracer and surfactant methods), as well as provide support for theoreticians and numerical modelers. Recent advances in experimental techniques have made it possible to characterize microscale phase distributions and pore geometry in porous media [*Wildenschild et al.*, 2002]. In particular, nondestructive synchrotron based X-ray computed microtomography allows 3D resolution of individual pores and interfaces at the micron scale. This kind of resolution is difficult to obtain with conventional, yet more accessible, X-ray techniques, as discussed by *Wildenschild et al.* [2002]. The present paper presents the results of experiments conducted using the synchrotron based technique to study and quantify air-water flow through a glass bead porous medium.

2. Background

[8] A number of investigations, both experimental and numerical, have been carried out in an effort to understand better the microscale physical processes occurring in multiphase porous media flow. Some of these investigations have been specifically designed to explore the physical

relationship between capillary pressure, saturation, and interfacial area.

2.1. Numerical Models

[9] A variety of numerical modeling techniques have been applied to the problem of subsurface multiphase flow; ranging from pore network models [e.g., *Lowry and Miller*, 1995; *Reeves and Celia*, 1996; *Kawanishi et al.*, 1998; *Dahle and Celia*, 1999; *Or and Tuller*, 1999; *Held and Celia*, 2001], to Lattice-Boltzmann simulations [*Coles et al.*, 1998; *Hazlett et al.*, 1998; *Pan et al.*, 2001, 2004], to investigations based on idealized sphere packings [*Hilpert and Miller*, 2001; *Dalla et al.*, 2002], as well as work done using simulated annealing algorithms [*Silverstein and Fort*, 2000a, 2000b, 2000c; *Berkowitz and Hansen*, 2001]. Numerical simulations provide a means by which pore-scale properties of interest, such as interfacial area, mass transfer, films, and wettability, can be researched.

[10] Numerical experiments have been used to gain insight into the three-dimensional physical formulation of the system at the microscale. Pore-scale network models allow explicit calculations of interfacial areas, capillary pressures, saturations, and relative permeabilities. They represent the pore space with geometric approximations to individual pore elements while maintaining the interconnectedness and random size distribution of a natural porous medium [e.g., *Lowry and Miller*, 1995; *Reeves and Celia*, 1996; *Held and Celia*, 2001]. Pore-scale models have been developed for quasi-static situations where the stability of the interface, dictated by the Young-Laplace equation (4), governs the fluid displacement:

$$p^c = \frac{2\gamma^{wn}\cos\theta}{R_{eff}}, \tag{4}$$

where p^c is the microscale capillary pressure, γ^{wn} is the wetting-nonwetting interfacial tension, θ is the contact angle between the wetting phase and the solid, and R_{eff} is the effective radius at the top of the meniscus. *Reeves and Celia* [1996] used a quasi-static pore network model to test the hypothesis that the interfacial area is a unique function of capillary pressure and saturation. *Reeves and Celia* [1996] demonstrated that, indeed, there is a strong functional dependence of capillary pressure on the fluid-fluid interfacial area. Also important is the fact that, while the fluid-fluid interfacial area is a unique function of capillary pressure and saturation [*Reeves and Celia*, 1996; *Held and Celia*, 2001], due to the convex nature of the curves produced, capillary pressure is not a unique function of saturation and interfacial area. Recent work has been done to develop a dynamic pore network model to simulate transient flow in porous media, rather than tracking equilibrium positions [*Dahle and Celia*, 1999]. However, this model has yet to be used to compute interfacial areas.

[11] *Hilpert and Miller* [2001] have used a pore morphology approach to model quasi-static drainage. A digital representation of a porous medium was obtained using a sphere-packing algorithm [*Yang et al.*, 1996] that requires only grain-size distribution and porosity as input parameters. *Dalla et al.* [2002] used the drainage simulator [*Hilpert and Miller*, 2001] to generate digital equilibrium phase distributions. Interfaces were approximated by a triangular mesh, which was created using the modified marching cubes algorithm. Interfacial area measurements were then determined from the mesh.

[12] Simulated annealing techniques have been used to analyze water distribution in a variably saturated porous medium [*Silverstein and Fort*, 2000a, 2000b, 2000c; *Berkowitz and Hansen*, 2001]. The goal of the simulated annealing method is to minimize the total interfacial free energy for a given saturation. First, the desired pore space is digitized and, based on a prescribed saturation, randomly seeded with a number of water filled voxels. Randomly generated swaps between air and water voxels are proposed, and the resultant energy change is calculated. Eventually, the total interfacial free energy of the system will reach a satisfactory minimum, and the interfacial area corresponding to the given saturation can be computed.

[13] Another avenue of numerical research involves the application of Lattice-Boltzmann (LB) models to subsurface flow. LB techniques approximate microscale Navier-Stokes flow and interfacial physics. LB models simulate flow by describing the movement and collisions of particles on a lattice [*Pan et al.*, 2001] while at the same time conserving mass and momentum [*Hazlett et al.*, 1998]. Because LB models are capable of handling arbitrarily complex boundary conditions, they provide a convenient means to simulate both single phase and multiphase flow in a true porous medium. Recently, *Pan et al.* [2004] developed a LB model to simulate three-dimensional multiphase (water and tetrachloroethylene) flow in an idealized sphere packing, consisting of eight spheres of equal diameter packed in a cubic lattice structure. They also modeled flow through a simulated porous medium. The simulated medium was based on a random sphere packing generated using parameters derived from NAPL-water displacement experiments reported in *Hilpert and Miller* [2001]. They then compared their computed results for the capillary pressure-saturation relationship to an existing data set [*Hilpert and Miller*, 2001]. The experimental and numerical results are similar.

2.2. Experimental Background

[14] Interest in quantitatively measuring the interfacial areas present in a subsurface multiphase flow system continues to increase as both theoretical developments and experimental observations illustrate that interfacial area is a key parameter in subsurface flow and transport. While phase volume fractions can be determined experimentally via a simple mass balance, no information is obtained concerning the fluid distribution in the sample. New techniques are being used to investigate saturation distributions in small porous medium samples. These techniques include gamma ray attenuation [e.g., *Saba et al.*, 2001], time domain reflectometry (TDR) [e.g., *Noborio*, 2001], magnetic resonance imaging [e.g., *Johns and Gladden*, 1999, 2000, 2001], and X-ray computerized microtomography [e.g., *Auzerais et al.*, 1996; *Coles et al.*, 1998; *Wildenschild et al.*, 2002, 2005; D. Wildenschild et al., Image processing of grey-scale x-ray tomographic data using cluster analysis–based segmentation: A hydrologic application, submitted to *Vadose Zone Journal*, 2004, hereinafter referred to as Wildenschild et al., submitted manuscript, 2004].

[15] Although phase volume fractions and distributions can be found using these techniques, relatively little has

been done to accurately determine specific interfacial areas, which are crucial to describing multiphase flow dynamics in porous media. *Karkare and Fort* [1996] were the first to develop a new experimental technique to measure the air-water interfacial area in unsaturated porous media. The method consisted of a horizontal column packed either with sand or glass beads and saturated to a specified level. A surfactant (1-tetradecanol) was added to half the column. When the surfactant reached a critical concentration, a pressure difference was set up which induced flow from one half of the column to the other. Because the surfactant chosen spreads as a solid monolayer at the air-water interface, the interfacial area can be computed as the number of molecules of surfactant required to initiate flow multiplied by the area occupied by each molecule at the interface.

[16] A significant portion of the work done estimating interfacial areas has focused on gaseous [e.g., *Kim et al.*, 1999; *Costanza-Robinson and Brusseau*, 2002] and aqueous [e.g., *Kim et al.*, 1997; *Saripalli et al.*, 1997; *Annable et al.*, 1998; *Rao et al.*, 2000] interfacial tracer techniques. Interfacial tracer methods rely on steady state effluent break through curves to compute a surface reactive tracer (for example, sodium dodecylbenzene sulfonate (SDBS) for aqueous systems and decane for gaseous systems) travel time and a nonreactive tracer travel time. On the basis of the travel times computed for a given saturation, a retardation factor is determined. Together with the adsorption coefficient for the reactive tracer, the retardation factor is used to calculate the air-water interfacial area. Recently, modifications have been made to the interfacial tracer technique using a mass balance that take into account the total reactive tracer mass at various cross sections of the column [e.g., *Anwar et al.*, 2000; *Schaefer et al.*, 2000].

[17] While all of these techniques [*Kim et al.*, 1997; *Saripalli et al.*, 1997; *Kim et al.*, 1999; *Anwar et al.*, 2000; *Rao et al.*, 2000; *Schaefer et al.*, 2000; *Costanza-Robinson and Brusseau*, 2002] provide an estimate of interfacial area, they do not explicitly enhance understanding of the internal structure of the porous medium; for example, how the phases distribute themselves, where the interfaces are, and how the fluid-fluid interfacial area changes as the saturation changes. Imaging techniques, such as photoluminescent volumetric imaging (PVI) used by *Montemagno and Gray* [1995], allow the internal structure of the porous medium to be seen at a number of equilibrium fluid configurations. Their experimental setup consisted of a small sample of crushed silica, simulating a natural sand, and two immiscible fluids with optical refractive indices matched to fused silica. The fluids were doped with fluorophores, which selectively gather at interfaces in the system. The fluorophores were excited with laser light, thereby allowing the internal structure of the system to be seen. Sample sizes up to 125 mm^3 were scanned with resolutions of better than 0.8 μm. Unfortunately, no quantitative image analysis has been performed with these experiments. Additionally, the PVI method is limited by the precise optical qualities necessary in the medium being imaged, thus restricting the number of systems that may be investigated. *Johns and Gladden* [1999, 2000] have used magnetic resonance imaging (MRI) to investigate NAPL dissolution and mobilization in porous media. They imaged a 35-mm-long section of a 400-mm-tall column with a 46 mm internal diameter. From the images collected, the geometric evolution of the NAPL-water interfaces can be observed over time. The column was packed with 5mm diameter glass ballotini and the three-dimensional images that resulted had a resolution of 390 μm. They demonstrated that, as intuitively expected, the velocity of the water flushed through the system greatly influences the dissolution process of the NAPL, thus impacting the evolution of the interfacial area distribution. However, the 390 μm resolution is too coarse to accurately compute interfacial areas.

[18] Recently, *Yu et al.* [2001] investigated fluid-fluid interfacial area using optical lithography to create a 2D etched glass micromodel. In this technique, a prescribed pore space is transferred onto a photosensitive polymer layer, called photoresist, using a visible light image. The portion of the photoresist exposed to light becomes soluble in a special developer solution, while the unexposed portion of the photoresist remains insoluble, resulting in a negative image of the original light pattern. The photoresist is then fixed between glass plates, with inlet and outlet holes located in the top plate. The sample is initially saturated with one phase, and then drained as a second fluid invades. Video microscopy is used to image the micromodel during displacement, and pressure measurements are made at both the inlet and outlet. Specific fluid-fluid interfacial areas were calculated as the line length per area and plotted, along with saturation, as a function of the capillary pressure. The two-dimensional micromodel experiments verify the strong dependence of the capillary pressure, p^c, on fluid-fluid interfacial area, a^{wn}, as well as saturation, s^w. The study shows that the hysteretic feature of the $p^c - s^w$ relationship is eliminated when the fluid-fluid interfacial area is included as a state variable, lending strong support to the conjecture [*Hassanizadeh and Gray*, 1993] that the interfacial area is the most influential of the independent variables missing from the capillary pressure functional dependence, and that the hysteresis found in $p^c - s^w$ curves is indeed an artifact of projecting a unique $p^c - s^w - a^{wn}$ curve onto the $p^c - s^w$ plane. While the micromodel study provides interesting results, they are for a two-dimensional model and limited saturation range. It is important to continue this work and determine if the same results are obtained for three-dimensional glass bead and, eventually, natural soil samples.

[19] Recent research conducted by *Wildenschild et al.* [2002, 2005; Wildenschild et al., submitted manuscript, 2004] uses X-ray computed microtomography (CMT) to obtain pore-scale images of soil samples and glass beads. Given the high resolution of the images obtained (pixel sizes ranging from 5.0 μm to 20 μm), the noninvasive nature of CMT, and recent advances in quantitative image analysis, the technique presents a promising avenue of research for accurate determination of interfacial areas and curvatures.

3. Experimental Approach and Setup

[20] The experiments presented here were conducted at the GeoSoilEnviro Consortium for Advanced Radiation Sources (GSECARS) bending magnet beamline, Sector 13, Advanced Photon Source (APS), Argonne National

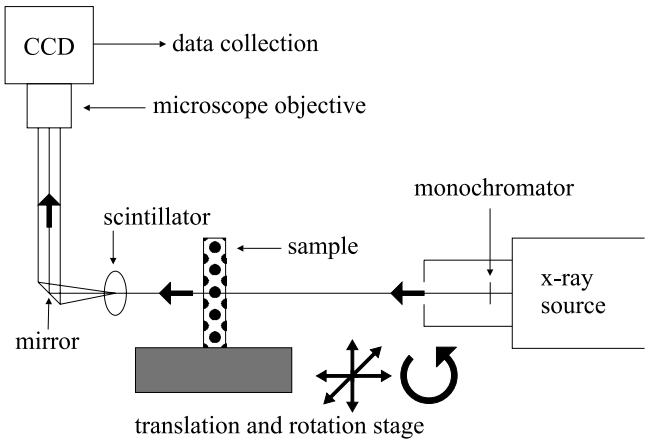

Figure 1. Beamline setup at GSECARS, Sector 13, Advanced Photon Source, Argonne National Laboratory.

Laboratory. With the exception of the camera (MicroMAX, 5 MHz, CCD camera) and monochromator (Si(111)), the experimental setup (Figure 1) used to obtain the three-dimensional images is the same as that described for rate dependence experiments on sand conducted by *Wildenschild et al.* [2002, 2005; Wildenschild et al., submitted manuscript, 2004]. Updated data collection hardware and software allowed for ~3 times faster scan times per 3D volume (~10 min). Images were taken of a 5 mm vertical section of a 7.0 cm long, 7.0 mm internal diameter pressure cell. The column was packed with soda lime glass beads (ρ = 2.50 g/cm^3). The size distribution of the glass beads is given in Table 1. The sample was packed to a porosity of 34%. Glass beads were chosen as the porous medium in order to reduce image processing challenges. The smooth surfaces of the beads were a benefit as was the absence of mineralogical impurities typically present in sand. A membrane permeable to the wetting phase separated the bead pack from the water reservoir, while the top of the sample was open to the atmosphere. The water used to saturate the sample was doped with KI (1:6 KI:H_2O mass ratio), and the sample scanned at 33.3 keV, just above the peak photoelectric absorption for iodine (~33.2 keV), in order to make the water phase distinguishable from the air phase. The resolution of the images obtained is 17 microns per voxel. Figure 2 shows a lateral cross section of the column. The white regions (highest attenuation) are the KI doped water phase; the gray regions are the beads; and the black regions (lowest attenuation) indicate space occupied by the air phase.

[21] The sample was initially packed with dry loose beads, and subsequently saturated on a primary imbibition curve. Images were taken at regular intervals throughout primary imbibition and drainage, and two cycles of secondary imbibition and drainage. Flow was induced via the use of a Harvard Apparatus, Inc., Model 44 programmable, electronic, syringe pump connected to the wetting phase reservoir. In order to image the sample, the pump was stopped, and the sample was allowed to stand for 10 min to permit the fluid to stop moving. Imaging of the sample then took approximately 10 more min to complete. Primary imbibition and drainage rates, as well as those for the first secondary imbibition and drainage cycle, were 0.25 mL/hr (1.8×10^{-4} cm/s). A flow rate of 2.0 mL/hr (1.4×10^{-3} cm/s) was selected for the third of the imbibition/drainage cycles. Pressure transducers connected to a laptop recorded pressure measurements at 2 s intervals. Water phase pressure was measured directly above and below the imaged region, as well as in the fluid reservoir. The pressure transducers located in the sample can be seen in Figure 3. Pressure measurements were zeroed to the top of the sample holder.

Table 1. Size Distribution of Porous Medium

% Weight	Diameter, mm
30	1–1.4
35	0.850
35	0.600

4. Image Analysis

[22] A cluster analysis is run on the partially saturated images, as well as the dry image. In the dry image, the cluster analysis creates a binary volume that separates air and solids. In the partially saturated image, a binary volume that separates air and solid+water is created. A 3 × 3 × 3 kernel median filter is used to smooth edges and remove salt and pepper noise from the binary images. The binary dry bead volume is then overlain on the binary partially saturated volume to generate segmented images in which each pixel is labeled as air, water, or solid (see Wildenschild et al. (submitted manuscript, 2004) for details). A subsection of 300 × 301 × 292 voxels (Figure 4) is taken from the fully segmented volume (650 × 650 × 650 voxels). This is done to minimize the influence of wall effects in the data extracted from the images. All subsequent data are

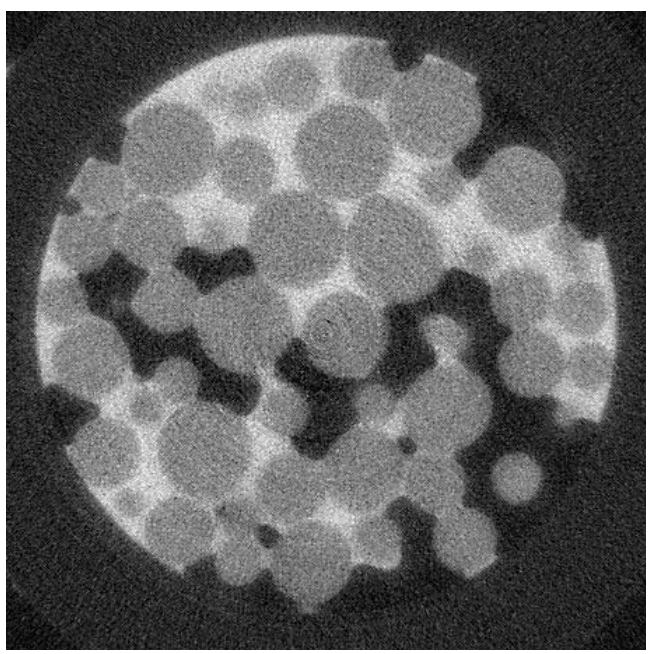

Figure 2. Two-dimensional (2-D) slice through glass bead column. Lightest (white) regions are water, gray regions are beads, and the darkest (black) regions are air.

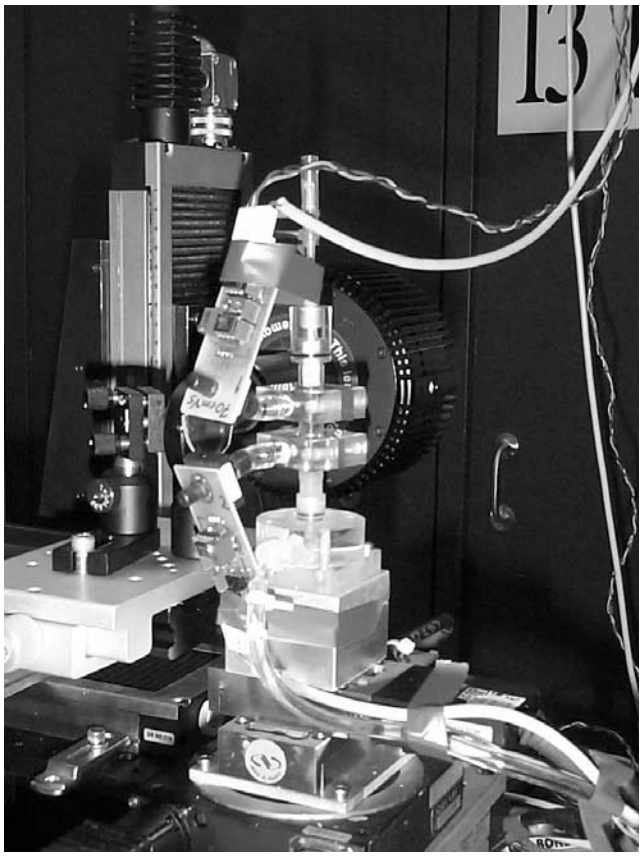

Figure 3. Photo of glass bead column mounted in the beam line. Pressure transducers are connected just above and below the imaged region as well as in the fluid reservoir (out of view). See color version of this figure in the HTML.

computed using this segmented subset of data. Saturations are determined using the routine described by Wildenschild et al. (submitted manuscript, 2004); the voxels belonging to each phase are counted and the wetting phase saturation determined as the percentage of air and water voxels belonging to the water phase.

[23] A commercial image analysis program, Amira™, is used to obtain interfacial area measurements. While it is possible to analyze the gray-scale data using this program, the overlap of the water and solid phases in the gray-scale histogram requires the user to select a threshold value to locate the wetting-nonwetting, wetting-solid, and nonwetting-solid interfaces in any given volume. Since these values are selected by the user and shift slightly from volume to volume as the image intensity values change, a more consistent approach is to consider the segmented images that were used to determine the saturation values. The data is first resampled by a factor of three using a triangular filter. This is done to decrease the nonphysical pixelation of the data which results in overestimates of the surface area. This pixelation of the data results in a smooth curve being represented as right angle straight line segments (stair steps). Amira uses a modified marching cubes algorithm to generate a triangular mesh representing the desired surface. Table 2 gives the results obtained applying this same process to calculate the surface area of a sphere. While the error continues to decrease as larger resample factors are used, finer features of the data set are smoothed away, resulting in a loss of information. A resample factor of three was chosen as the best compromise between a highly pixilated image and an overly decimated image.

[24] After resampling the segmented data, isosurfaces are generated. From these isosurfaces the total specific wetting phase surface area (a^w) and total specific nonwetting phase surface area (a^n) can be computed for each volume (Figures 5a and 5b). The specific solid phase surface area (a^s) is computed from the dry image (Figure 5c). The specific wetting-nonwetting interfacial area (a^{wn}) can then be calculated according to [e.g., *Dalla et al.*, 2002]

$$a^{wn} = \frac{1}{2}(a^w + a^n - a^s). \tag{5}$$

5. Representative Elementary Volume (REV) Analysis

[25] While there are many scales of interest in the field of subsurface multiphase flow, of particular interest in this study are macroscopic variables; that is variables that can be associated with a representative elementary volume (REV) [*Bear*, 1972]. Macroscopic variables are typically defined as averages of microscopic variables over a REV. *Dullien* [1992] qualitatively states that a macroscopic porous medium may be defined by a smooth porosity variation as a function of the sample volume. As there is no quantitative, universal measure for the size of an REV, it is necessary to determine whether or not the data collected and analyzed in this study satisfy the REV requirement. Specifically, we wished to ascertain that the subsection of the full volume used to collect the porosity, saturation, and interfacial area data presented here was adequate for all three properties of interest.

[26] The average grain size for the distribution of beads used in these experiments is 0.8675 mm and was computed as the weighted average of the grain sizes with 30% of the beads taken to have a diameter of 1.2 mm (Table 1). The

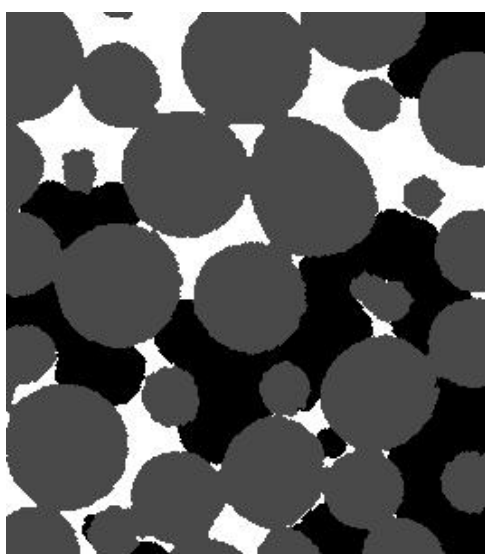

Figure 4. Segmented subset of data. White is water, gray is beads, and black is air.

Table 2. Error Analysis for Surface Area of a Sphere

Radius, voxels	Resampling Factor	Analytical Surface Area, voxels^2	Computed Surface Area, voxels^2	% Error
25	no resampling[a]	7853.975	8907.2	13.41
	2		8292.8	5.59
	3		8107	3.22
	4		8035.3	2.31
	5		7939.7	1.09
	6		7799.5	−0.69
50	no resampling	31415.900	34971.9	11.32
	2		32796.7	4.40
	3		32206.9	2.52
	4		32021.3	1.93
	5		31878.9	1.47
	6		31739.6	1.03
75	no resampling	70685.775	78099	10.49
	2		73422	3.87
	3		72200	2.14
	4		71837	1.63
	5		71595	1.29
	6		71408	1.02

[a]No filter was applied to the data.

dimensions of the subsection of data analyzed are 4.522 mm, 5.117 mm, and 4.964 mm in the x, y, and z directions, respectively. This corresponds to respective average grain diameters in the x, y, and z directions of 5.2, 5.9, and 5.7. Figures 6a and 6b illustrate the variation of saturation and porosity as a function of the size of the averaging volume used. Similarly, Figure 6c shows the specific surface area as a function of domain size. As expected, the porosity, saturation, and specific interfacial area are erratic for small domain sizes. It can be seen for all quantities of interest that the REV size is independent of saturation and location on the hysteresis loop. The wetting fluid saturation and specific interfacial area values exhibit similar behavior and appear to reach steady values at the same size. This was also found to be the case in the pore network study of *Reeves and Celia* [1996]. At the outer limits of the domain, the saturation values computed are varying ±0.5%, and the specific interfacial area values are varying ±5%. *Bear* [1972] states that in the range of an REV, small amplitude fluctuations in the properties of interest are to be expected and are due to the random distribution of pore sizes in the neighborhood of the centroid of the REV. Given the small range of variation in the porosity, saturation, and interfacial area values at the outer limit of the domain size, it seems reasonable to conclude that we are likely at the lower limits of what may be considered an acceptable REV.

6. Results and Discussion

[27] Results obtained from the April 2002 experimental run at the APS may be seen in Figures 7a–7c. Figure 7a shows the capillary head as a function of saturation; a traditional hysteresis loop. The column was fully saturated at the beginning of primary drainage. The entry pressure for primary drainage can be seen to be approximately −5 cm. The entry pressure for the secondary hysteresis loop is about −4 cm, noticeably lower than that observed for primary drainage. Very low residual wetting phase saturations were obtained; down to 4.3% on primary drainage. *Dullien* [1992] reports residual wetting phase saturations ranging from 1.4% to 9% in glass bead packs depending on surface roughness. No difference was observed between the second imbibition and drainage cycle (0.25 mL/hr) and the third imbibition and drainage cycle (2.0 mL/hr). Figure 7b shows the specific wetting-nonwetting (wn) interfacial area as a function of saturation. The small negative interfacial areas observed at the beginning of primary drainage correspond to full saturation and are likely due to numerical error in the image analysis routine, or misidentification of pixels as fluid-fluid interfaces when, in fact, there are none. The shape of the observed curve in Figure 7b is similar to that hypothesized by *Hassanizadeh and Gray* [1993]. Films were not included in this analysis. Therefore as expected, a^{wn} increases as the saturation decreases, reaches a maximum ($0.20 < s^w < 0.35$), and then decreases as the water saturation continues to decrease. This shape also appears in the work of *Reeves and Celia* [1996]. The maximum a^{wn} values observed in imbibition are lower than those seen in drainage. On the basis of consideration of flow in a simple

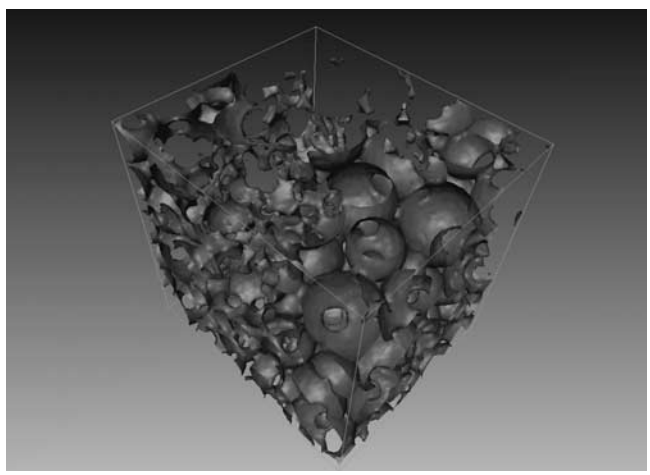

Figure 5a. Total wetting phase surface for GB_32 (s^w = 0.72). See color version of this figure in the HTML.

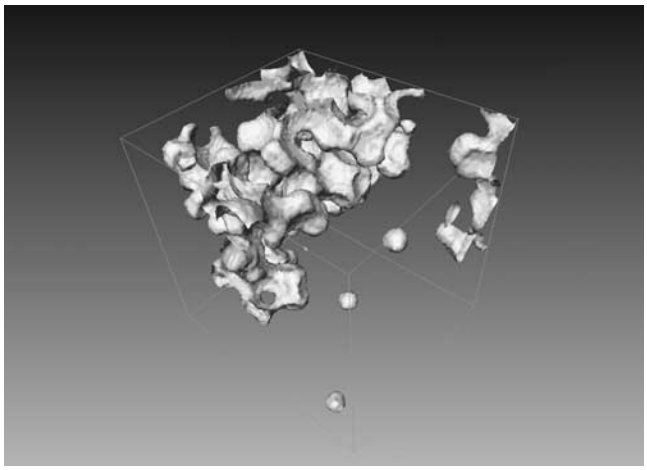

Figure 5b. Total nonwetting phase surface. See color version of this figure in the HTML.

capillary tube, this would be expected; in imbibition, the advancing interface is flatter (less area); whereas in drainage, the receding interface is stretched out (greater area). Figure 7c shows the capillary pressure as a function of area. The shape of the curves differs somewhat from that speculated on by *Hassanizadeh and Gray* [1993]. Ideally, this data set would have served as a test to the hypothesis that including the *wn* interfacial area in the functional form of the capillary pressure would eliminate, or significantly reduce, the hysteresis observed between imbibition and drainage cycles. However, not enough data points were collected to confidently plot a $p^c - s^w - a^{wn}$ surface.

6.1. Comparison to Numerical Experiments

[28] Using a pore network model, *Reeves and Celia* [1996] found a relationship between a^{wn} and s^w very similar in shape to that found in the present study. However, they observed a maximum wetting phase saturation of 74.4% on secondary imbibition, compared to an observed 92.1% maximum in the glass bead column being studied. Owing to difficulties in determining the rules for snap off, the network model was drained to a zero residual wetting phase saturation, while the lowest measured saturation in the glass beads was 4.3%. *Reeves and Celia* [1996] note a maximum a^{wn} occurring at s^w = 27.1% for primary drainage, s^w = 38.1% for main imbibition, and s^w = 29.5% for main drainage. This compares to experimentally observed maximum a^{wn} values occurring at measured saturations of s^w = 23.2%, s^w = 24.4%, and s^w = 33.5% for primary drainage, main imbibition, and main drainage, respectively. The maximum interfacial area value for secondary drainage occurs at a lower saturation for the pore network study than that observed in the glass bead column. This may be due to the fact that no space is provided for pendular rings in the pore network model. Pendular rings provide a rather significant contribution to saturation and specific interfacial area on secondary drainage and beyond (Figure 8). How-

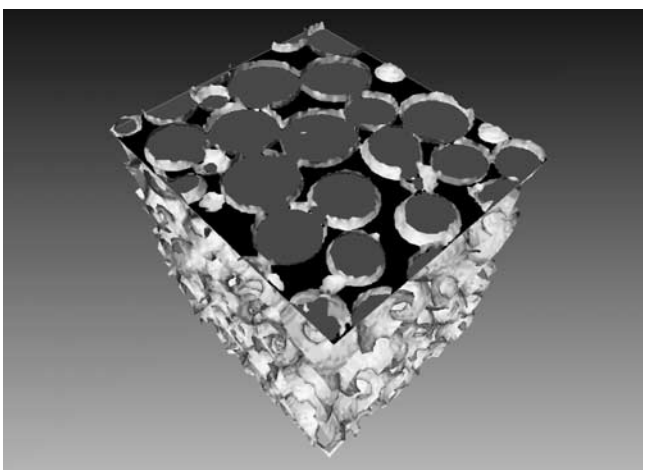

Figure 5c. Total solid phase surface. The 2-D slice illustrates the match between the IDL segmented volume and the Amira isosurface generated from it. See color version of this figure in the HTML.

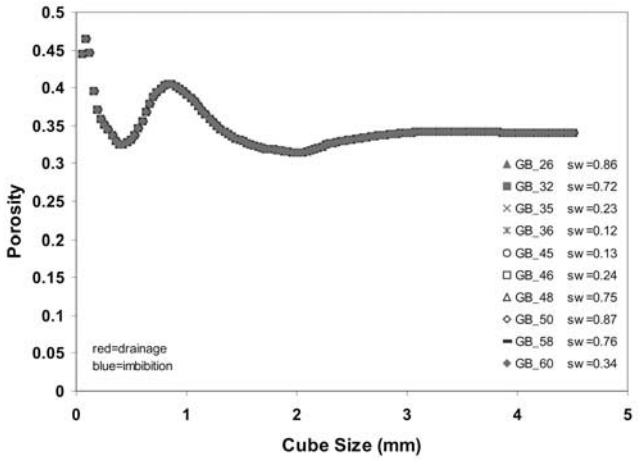

Figure 6a. Porosity as a function of representative elementary volume (REV) size for points on primary drainage, secondary imbibition, and secondary drainage. The porosity was obtained by determining the number of pixels that belonged to the air and water phase as a percentage of the total number of pixels. This was done over a range of saturations to ensure consistency of the image analysis routine. See color version of this figure in the HTML.

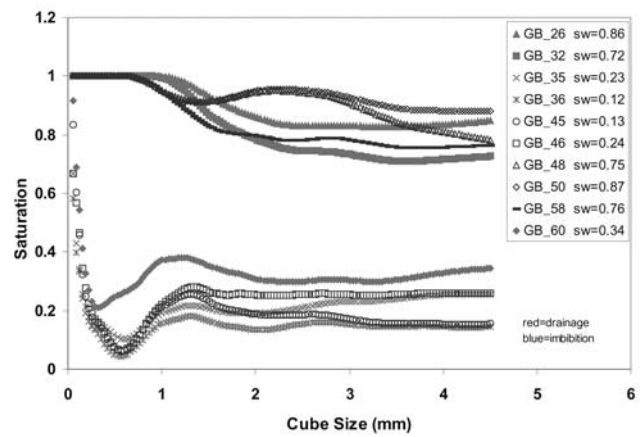

Figure 6b. Saturation as a function of REV size. See color version of this figure in the HTML.

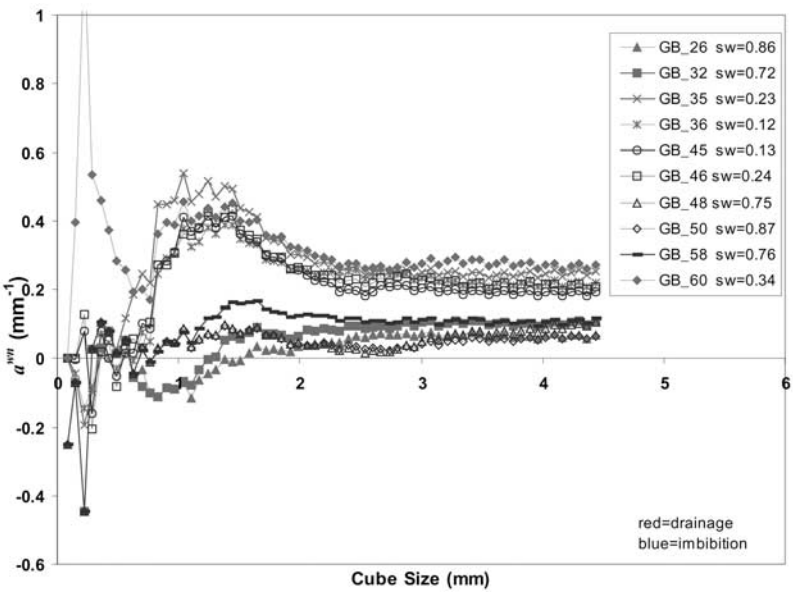

Figure 6c. Wetting-nonwetting interfacial area as a function of REV size. See color version of this figure in the HTML.

ever, the number of experimental data points is relatively small, and it should be kept in mind that actual maximum a^{wn} may occur at saturations other than those observed. Neither the pore network model nor the experimental values presented here include films in the measurement of a^{wn}.

[29] *Dalla et al.* [2002] present the results of applying a modified marching cubes algorithm to analyze results obtained using the pore drainage simulator of *Hilpert and Miller* [2001]. They, again, find a shape similar to that shown in Figure 7b for the relationship between a^{wn} and s^w. The maximum value of a^{wn} occurs at $s^w = 0.21$ for primary drainage. In addition, *Dalla et al.* [2002] found a relationship between capillary head and a^{wn} very similar to that shown in 7c.

[30] *Berkowitz and Hansen* [2001] used a simulated annealing algorithm to investigate flow in a Fountainbleu sandstone. Their results also show a^{wn} increasing as the saturation decreases, reaching a maximum at $s^w \approx 0.30$, and then decreasing as $s^w \rightarrow 0$. The pore space discretization used in this study is coarse relative to the thickness of a film, and the algorithm does not approach a thin film covering the grain surface at low saturations, which means that $a^{wn} \rightarrow 0$ as $s^w \rightarrow 0$ (B. Berkowitz, Weizmann Institute of Science, personal communication, 2003). This is in contrast to the results found by *Silverstein and Fort* [1997, 2000a] who also used a simulated annealing algorithm. Their model showed a^{wn} continuing to increase as $s^w \rightarrow 0$. This is due to the fact that they have assumed the solid phase to be entirely covered by a thin film of water. While the film thickness is much less than the dimension of a single voxel, the presence of the film is accounted for in the choice of interfacial tension values used as inputs to the model.

6.2. Comparison to Other Experiments

[31] Contrary to the results found in this study, other experimental techniques used to measure interfacial area, including surfactant methods used to study media such as sand and glass beads [*Karkare and Fort*, 1996; *Silverstein and Fort*, 1997] and interfacial tracer methods used to study porous materials including sand, glass beads, and field sites [e.g., *Kim et al.*, 1997; *Saripalli et al.*, 1997; *Kim et al.*, 1999; *Anwar et al.*, 2000; *Rao et al.*, 2000; *Schaefer et al.*, 2000; *Costanza-Robinson and Brusseau*, 2002], have all found that the fluid-fluid interfacial area continues to increase as $s^w \rightarrow 0$. This does not indicate that any one of these methods is necessarily wrong. Rather, there is a lack of understanding concerning which interfaces are being detected in any of these techniques. Indeed, discrepancies exist within the interfacial tracer community based on whether an aqueous phase or gaseous phase tracer is used. *Costanza-Robinson and Brusseau* [2002] suggest that this may be due to the fact that aqueous phase surface reactive tracers have limited access to adsorbed water, and therefore fail at lower saturations. In comparison, they hypothesize

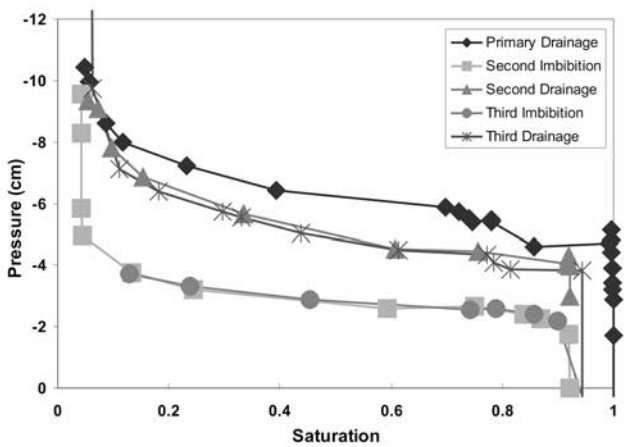

Figure 7a. Two-dimensional projections of $p^c - s^w - a^{wn}$ relationship. See color version of this figure in the HTML.

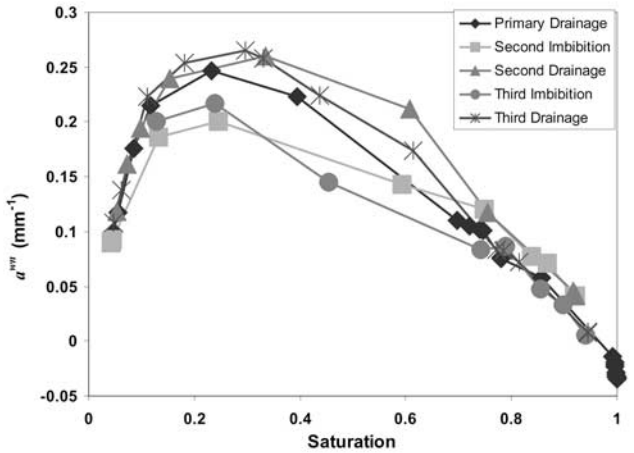

Figure 7b. Slightly negative interfacial areas are due to the misidentification of a small number of pixels as air in a fully saturated volume or numerical error in the image analysis routine. See color version of this figure in the HTML.

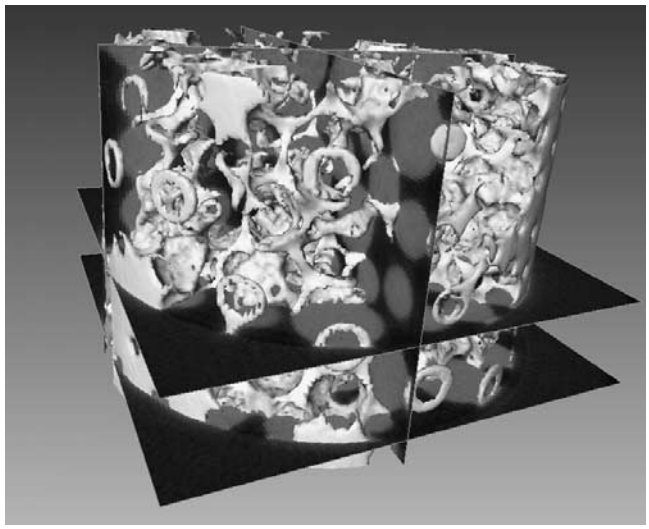

Figure 8. Pendular rings; $s^w = 0.23$, $a^{wn} = 0.25$ mm^{-1}. See color version of this figure in the HTML.

that the gaseous phase surface reactive tracers are capable of accessing both the water accessible to advective flow as well as adsorbed water. It is unlikely that any of the interfacial tracer techniques are capable of measuring interfacial areas that are isolated (inaccessible to advective water or gas) [*Costanza-Robinson and Brusseau*, 2002]. Investigations that combine a direct measurement of interfacial area, such as that presented herein, with concurrent tracer experiments would allow us to determine which interfaces are measured in each technique. A greater understanding of how the interfacial tracer technique works could be to great advantage for practical applications given that interfacial tracers can be applied in the field [e.g., *Annable et al.*, 1998; *Anwar et al.*, 2000] whereas direct measurements, such as that presented here, cannot.

7. Summary and Critique

[32] Fully three-dimensional images of unsaturated flow through a glass bead column were obtained using synchrotron based X-ray microtomography. Primary drainage (0.25 mL/hr) as well as secondary imbibition and drainage (0.25 mL/hr and 2.0 mL/hr) cycles were investigated. No difference was observed between the 0.25 mL/hr and 2.0 mL/hr flow rates. The gray-scale images collected were segmented into phases, with each voxel being identified as belonging to the air, water, or solid phase. A commercial image analysis program, Amira, which uses a modified marching cubes algorithm to approximate a surface, was used to compute interfacial area values at various points on the imibition and drainage curves. As expected, interfacial area values were found to increase until a maximum was reached in the 20–35% saturation range, and then decrease as the saturation continued to zero.

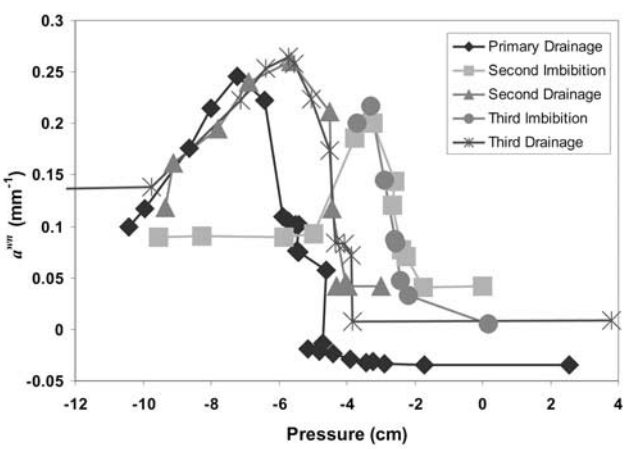

Figure 7c. Wetting-nonwetting interfacial area versus capillary pressure. See color version of this figure in the HTML.

[33] The presence of fluid films on the solid surfaces were not observed or accounted for in the experiments presented here. A film coating the solid surface would be in the range of angstroms to microns thick. This would require pushing the resolution limits of the experimental technique presented here to the very edge, with the likelihood that only relatively thick films would be detected. In addition, there is an experimental trade off between the size of the imaged region and the image resolution. Results were presented here which demonstrate that the region of the sample analyzed, with a resolution of 17 microns per pixel, was at the lower limits of the REV range. In order to obtain a better resolution, the size of the imaged region would have to be considerably smaller, meaning that the REV would have to be sacrificed in order to observe films that might be present in the system.

[34] $a^{wn} - s^w$ loops were compared to numerical studies and showed very good agreement with the pore network modeling of *Reeves and Celia* [1996] and the simulated annealing modeling of *Berkowitz and Hansen* [2001]. *Dalla et al.* [2002] presented results found using a pore drainage simulator that also agree with the general trend of the $a^{wn} - s^w$ as well as the $a^{wn} - p^c$ relationship. None of these numerical studies accounted for the presence of films. In addition, the experimental results presented here agree well with theoretical predictions put forth by *Hassanizadeh and Gray* [1993]. However, due to the relatively sparse nature of the data collected, it was not possible to test the uniqueness

of the $p^c - s^w - a^{wn}$ surface. It is also worth noting that the thermodynamically based theory [e.g., *Gray et al.*, 2002] does not specifically account for the presence of films.

[35] Our experimental results were also compared to experimental results found by a number of researches using surfactant methods [*Karkare and Fort*, 1996; *Silverstein and Fort*, 1997] and interfacial tracer techniques [*Kim et al.*, 1997; *Saripalli et al.*, 1997; *Kim et al.*, 1999; *Anwar et al.*, 2000; *Rao et al.*, 2000; *Schaefer et al.*, 2000; *Costanza-Robinson and Brusseau*, 2002]. There is not a precise understanding of exactly which fluid-fluid interfaces are being measured by these techniques. However, they all display a monotonic increase in interfacial area with decreasing saturation. Further work should be done conducting complementary experiments that use the surfactant based and interfacial tracer methods along with direct measurement techniques such as synchrotron based X-ray microtomography.

Notation

D^s/Dt macroscopic material time derivative with respect to the solid phase.
ε porosity.
ε^w volume fraction of the wetting phase.
x_s^{ws} wetted fraction of the solid surface.
L_s a positive coefficient.
p^c capillary pressure.
p^w wetting phase pressure.
p^n nonwetting phase pressure.
γ^{wn} wetting-nonwetting interfacial tension.
J_{wn}^w mean macroscale curvature.
a^{wn} wetting-nonwetting specific interfacial area.
a^w specific wetting phase interfacial area.
a^n specific nonwetting phase interfacial area.
a^s specific solid phase interfacial area.
s^w wetting phase saturation.
θ microscale contact angle between the wetting phase and the solid.
R_{eff} effective radius.

[36] **Acknowledgments.** This work was supported by a National Science Foundation (NSF) Graduate Research Fellowship, NSF grants DMS-0327896 and EAR-0337535, and a grant from the Danish Technical Research Council. W.G.G. acknowledges partial support of his effort on this work by NSF through DMS-0112069 to the Statistical and Applied Mathematical Sciences Institute in Research Triangle Park. Portions of this work were performed at GeoSoilEnviroCARS (Sector 13), Advanced Photon Source (APS), Argonne National Laboratory. GeoSoilEnviroCARS is supported by the National Science Foundation-Earth Sciences (EAR-0217473), Department of Energy-Geosciences (DE-FG02-94ER14466) and the State of Illinois. Use of the APS was supported by the U.S. Department of Energy, Basic Energy Sciences, Office of Energy Research, under contract W-31-109-Eng-38.

References

Annable, M. D., J. W. Jawitz, P. S. C. Rao, D. P. Dai, H. Kim, and A. L. Wood (1998), Field evaluation of interfacial and partitioning tracers for characterization of effective NAPL-water contact areas, *Ground Water*, *36*, 495–503.

Anwar, A. H. M. F., M. Bettahar, and U. Matsubayashi (2000), A method for determining air-water interfacial area in variably saturated porous media, *J. Contam. Hydrol.*, *43*, 129–146.

Auzerais, F. M., J. Dunsmuir, B. B. Ferréol, N. Martys, J. Olson, T. S. Ramakrishnan, D. H. Rothman, and L. M. Schwartz (1996), Transport in sandstone: A study based on three-dimensional microtomography, *Geophys. Res. Lett.*, *23*, 705–708.

Bear, J. (1972), *Dynamics of Fluids in Porous Media*, Dover, New York.

Bennethum, L. S. (1994), Multiscale, hybrid mixture theory for swelling systems with interfaces, *Tech. Rep. 259*, Cent. for Appl. Math. Purdue Univ., West Lafayette, Ind.

Berkowitz, B., and D. P. Hansen (2001), A numerical study of the distribution of water in partially saturated porous rock, *Transp. Porous Media*, *45*, 303–319.

Coles, M. E., R. D. Hazlett, P. Spanne, W. E. Soll, E. L. Muegge, and K. W. Jones (1998), Pore level imaging of fluid transport using synchrotron X-ray microtomography, *J. Petrol. Sci. Eng.*, *19*, 55–63.

Costanza-Robinson, M. S., and M. L. Brusseau (2002), Air-water interfacial areas in unsaturated soils: Evaluation of interfacial domains, *Water Resour. Res.*, *38*(10), 1195, doi:10.1029/2001WR000738.

Dahle, H. K., and M. A. Celia (1999), A dynamic network model for two-phase immiscible flow, *Comput. Geosci.*, *3*, 1–22.

Dalla, E., M. Hilpert, and C. T. Miller (2002), Computation of the interfacial area for two-fluid porous medium systems, *J. Contam. Hydrol.*, *56*, 25–48.

Dullien, F. A. L. (1992), *Porous Media: Fluid Transport and Pore Structure*, 2nd ed., Academic, San Diego, Calif.

Gray, W. G. (1999), Thermodynamics and constitutive theory for multiphase porous-media flow considering internal geometric constraints, *Adv. Water Resour.*, *22*, 521–547.

Gray, W. G. (2000), Macroscale equilibrium conditions for two-phase flow in porous media, *Int. J. Multiphase Flow*, *26*, 467–501.

Gray, W. G., and S. M. Hassanizadeh (1989), Averaging theorems and averaged equations for transport of interface properties in multiphase systems, *Int. J. Multiphase Flow*, *15*, 81–95.

Gray, W. G., and S. M. Hassanizadeh (1998), Macroscale continuum mechanics for multiphase porous-media flow including phases, interfaces, common lines and common points, *Adv. Water Resour.*, *21*, 261–281.

Gray, W. G., A. Leijnse, R. L. Kolar, and C. A. Blain (1993), *Mathematical Tools for Changing Spatial Scales in the Analysis of Physical Systems*, CRC Press, Boca Raton, Fla.

Gray, W. G., A. F. B. Tompson, and W. E. Soll (2002), Closure conditions for two-fluid flow in porous media, *Transp. Porous Media*, *47*, 29–65.

Hassanizadeh, S. M., and W. G. Gray (1993), Thermodynamic basis of capillary pressure in porous media, *Water Resour. Res.*, *29*, 3389–3405.

Hazlett, R. D., S. Y. Chen, and W. E. Soll (1998), Wettability and rate effects on immiscible displacement: Lattice Boltzmann simulation in microtomographic images of reservoir rocks, *J. Petrol. Sci. Eng.*, *20*, 167–175.

Held, R. J., and M. A. Celia (2001), Modeling support of functional relationships between capillary pressure, saturation, interfacial areas and common lines, *Adv. Water Resour.*, *24*, 325–343.

Hilpert, M., and C. T. Miller (2001), Pore-morphology-based simulation of drainage in totally wetting porous media, *Adv. Water Resour.*, *24*, 243–255.

Imhoff, P. T., P. R. Jaffe, and G. F. Pinder (1994), An experimental study of complete dissolution of a nonaqueous phase liquid in saturated porous media, *Water Resour. Res.*, *30*, 307–320.

Johns, M. L., and L. F. Gladden (1999), Magnetic resonance imaging study of the dissolution kinetics of octanol in porous media, *J. Colloid Interface Sci.*, *210*, 261–270.

Johns, M. L., and L. F. Gladden (2000), Probing ganglia dissolution and mobilization in a water-saturated porous medium using MRI, *J. Colloid Interface Sci.*, *225*, 119–127.

Johns, M. L., and L. F. Gladden (2001), Surface-to-volume ratio of ganglia trapped in small-pore systems determined by pulse-field gradient nuclear magnetic resonance, *J. Colloid Interface Sci.*, *238*, 96–104.

Karkare, M. V., and T. Fort (1996), Determination of the air-water interfacial area in wet "unsaturated" porous media, *Langmuir*, *12*, 2041–2044.

Kawanishi, T., Y. Hayashi, P. V. Roberts, and M. J. Blunt (1998), Fluid-fluid interfacial area during two and three phase fluid displacement in porous media: A network model study, paper presented at GQ 98, International Conference and Special Seminars on Groundwater Quality: Remediation and Protection, Tubingen, Germany.

Kim, H., P. S. C. Rao, and M. D. Annable (1997), Determination of effective air-water interfacial area in partially saturated porous media using surfactant adsorption, *Water Resour. Res.*, *33*, 2705–2711.

Kim, H., P. S. C. Rao, and M. D. Annable (1999), Consistency of the interfacial tracer technique: Experimental evaluation, *J. Contam. Hydrol.*, *40, 79–94.*

Lowry, M. I., and C. T. Miller (1995), Pore-scale modeling of nonwetting-phase residual in porous media, *Water Resour. Res.*, *31*, 455–473.

Miller, C. T., M. M. Poirier-McNeill, and A. S. Mayer (1990), Dissolution of trapped nonaqueous phase liquids: Mass transfer characteristics, *Water Resour. Res.*, *26*, 2783–2796.

Montemagno, C. D., and W. G. Gray (1995), Photoluminescent volumetric imaging: A technique for the exploration of multiphase flow and transport in porous media, *Geophys. Res. Lett.*, *22*, 425–428.

Nambi, I. M., and S. E. Powers (2000), NAPL dissolution in heterogeneous systems: An experimental investigation in a simple heterogeneous system, *J. Contam. Hydrol.*, *44*, 161–184.

Noborio, K. (2001), Measurement of soil water content and electrical conductivity by time domain reflectometry: A review, *Comp. Electr. Agric.*, *31*, 213–237.

Or, D., and M. Tuller (1999), Liquid retention and interfacial area in variably saturated porous media: Upscaling from single-pore to sample-scale model, *Water Resour. Res.*, *35*, 3591–3605.

Pan, C. X., M. Hilpert, and C. T. Miller (2001), Pore-scale modeling of saturated permeabilities in random sphere packings, *Phys. Rev. E*, *64*, 066702.

Pan, C., M. Hilpert, and C. T. Miller (2004), Lattice-Boltzmann simulation of two-phase flow in porous media, *Water Resour. Res.*, *40*, W01501, doi:10.1029/2003WR002120.

Powers, S. E., L. M. Abriola, and W. J. Weber, Jr. (1992), An experimental investigation of nonaqueous phase liquid dissolution in saturated subsurface systems: Steady state mass transfer rates, *Water Resour. Res.*, *28*, 2691–2705.

Rao, P. S. C., M. D. Annable, and H. Kim (2000), NAPL source zone characterization and remediation technology performance assessment: Recent developments and applications of tracer techniques, *J. Contam. Hydrol.*, *45*, 63–78.

Reeves, P. C., and M. A. Celia (1996), A functional relationship between capillary pressure, saturation, and interfacial area as revealed by a pore-scale network model, *Water Resour. Res.*, *32*, 2345–2358.

Saba, T., T. H. Illangasekare, and J. Ewing (2001), Investigation of surfactant-enhanced dissolution of entrapped nonaqueous phase liquid chemicals in a two-dimensional groundwater flow field, *J. Contam. Hydrol.*, *51*, 63–82.

Saripalli, K. P., H. Kim, P. S. C. Rao, and M. D. Annable (1997), Measurement of specific fluid-fluid interfacial areas of immiscible fluids in porous media, *Environ. Sci. Technol.*, *31*, 932–936.

Schaefer, C. E., D. A. DiCarolo, and M. J. Blunt (2000), Determination of water-oil interfacial area during 3-phase gravity drainage in porous media, *J. Colloid Interface Sci.*, *221*, 308–312.

Silverstein, D. L., and T. Fort (1997), Studies in air-water interfacial area for wet unsaturated particulate porous media systems, *Langmuir*, *13*, 4758–4761.

Silverstein, D. L., and T. Fort (2000a), Prediction of air-water interfacial area in wet unsaturated porous media, *Langmuir*, *16*, 829–834.

Silverstein, D. L., and T. Fort (2000b), Incorporating low hydraulic conductivity in a numerical model for predicting air-water interfacial area in wet unsaturated particulate porous media, *Langmuir*, *16*, 835–838.

Silverstein, D. L., and T. Fort (2000c), Prediction of water configuration in wet unsaturated porous media, *Langmuir*, *16*, 839–844.

Wildenschild, D., J. W. Hopmans, C. M. P. Vaz, M. L. Rivers, and D. Rikard (2002), Using X-ray computed tomography in hydrology: Systems, resolutions, and limitations, *J. Hydrol.*, *267*, 285–297.

Wildenschild, D., J. W. Hopmans, M. L. Rivers, and A. J. R. Kent (2005), Quantitative analysis of flow processes in a sand using synchrotron based X-ray microtomography, *Vadose Zone J.*, in press.

Yang, A., C. T. Miller, and L. D. Turcoliver (1996), Simulation of correlated and uncorrelated packing of random size spheres, *Phys. Rev. E*, *53*, 1516–1624.

Yu, P., N. Giordano, T. Cheng, M. Mustata, W. Headley, D. Chen, N. Cooper, D. D. Nolte, and L. J. Pyrak-Nolte (2001), Experimental investigation of relative permeability upscaling from the micro-scale to the macro-scale, semiannual progress report, Dept. of Phys. Purdue Res. Found., West Lafayette, Ind., March.

B. S. B. Christensen, Environment and Resources, Technical University of Denmark, DK-2800 Lyngby, Denmark. (brc@er.dtu.dk)

K. A. Culligan and D. Wildenschild, Department of Geosciences, Oregon State University, Wilkinson Hall, Corvallis, OR 97331, USA. (kculliga@nd.edu; wildend@geo.oregonstate.edu)

W. G. Gray, Department of Environmental Science and Engineering, University of North Carolina, Chapel Hill, NC 27599-7400, USA. (wggray@unc.edu)

M. L. Rivers, Department of Geophysical Sciences, University of Chicago, 5734 S. Ellis Avenue, Chicago, IL 60637, USA. (rivers@cars.uchicago.edu)

A. F. B. Tompson, Geosciences and Environmental Technologies Division, L-208, Lawrence Livermore National Laboratory, Livermore, CA 94551, USA. (afbt@llnl.gov)